Open Ceramics 22 (2025) 100793

Contents lists available at ScienceDirect

Open Ceramics

journal homepage: www.sciencedirect.com/journal/open-ceramics

Microwave dielectric properties and microstructure of high entropy $(Mg_xCa_{0.6-x}Sr_{0.39}Ba_{0.01})ZrO_3$ ceramics

Huei-Jyun Shih [a,†], Chin-Tung Shih [b,†], Ying-Chieh Lee [a,b,*]

[a] Institute of Precision Electronic Components, National Sun Yat-Sen University, Kaohsiung 804, Taiwan
[b] Department of Electrical Engineering, National Sun Yat-Sen University, Kaohsiung 804, Taiwan

ARTICLE INFO

Keywords:
NPO dielectric material
ABO_3
Oxygen vacancy
dielectric properties

ABSTRACT

The synthesis and characterization of $Mg_xCa_{0.6-x}Sr_{0.39}Ba_{0.01}ZrO_3$ (x = 0.01, 0.03, and 0.05) ceramics using the solid-state method was investigated at varying sintering temperatures in this study. The results show that increasing MgO doping and higher sintering temperatures enhance the ceramic's bulk density, highlighting the sintering enhancement effect of MgO. However, excessive MgO doping exceeds the solubility limit, resulting in reduced density and the formation of secondary phases. Dielectric measurements reveal that the dielectric constant increases with MgO doping up to 1 % but decreases at higher concentrations. Ceramics sintered at 1350 °C exhibit optimal dielectric properties, including a high permittivity of 32.98 and a $Q \times f$ value of 22,012 at 8–9 GHz. These results demonstrate stable dielectric performance with minimal loss at high frequency due to Mg doping as a fifth cation. This behavior suggests that dielectric relaxation is associated with the high entropy effect.

1. Introduction

With the rapid development of communication technology, the demand for high-frequency multilayer ceramic capacitors (MLCCs) has surged dramatically [1]. However, the polarization mechanism in dielectric materials is highly dependent on the frequency of the applied electric field. As operating frequencies increase with high frequency and 5 G communication systems, dielectric materials must exhibit faster polarization, which requires shorter relaxation times. If the relaxation time exceeds the switching period of the electric field, dielectric relaxation will cause significant dielectric loss, leading to friction and heat buildup in devices. To meet the high-frequency requirements of next-generation MLCCs, many studies have focused on developing new dielectric materials with high dielectric constants, quality factors (Q factor), and resonant frequencies [2–3].

Perovskite barium strontium titanate (BST) ceramics are promising materials for use in the electronic components industry. The unique ABO_3 perovskite structure of BST series ceramics exhibits a remarkable ability to incorporate metallic species at either the A-site or B-site, such as calcium, strontium and magnesium [4–5]. Similarly, other ABO_3 perovskite ceramics, particularly zirconium-based perovskites, have been explored to improve mechanical properties, as seen in $Ca_{1-x}Sr_xZrO_3$ [6]. Due to their low temperature coefficients and low dielectric loss, $CaZrO_3$, $SrZrO_3$, $BaZrO_3$, and their combinations have gained significant attention in the development of NPO microwave dielectric ceramics [7,8]. Notably, Y. C. Lee et al. reported that $Ca_{0.6}Sr_{0.39}Ba_{0.01}ZrO_3$ ceramics sintered at 1450 °C for 2 hours, achieved a permittivity of 29, a dielectric loss (tanδ) of 2.7 × 10^{-4}, and an insulation resistance (IR) of 2.6 × 10^{12} Ω [6]. Consequently, this study focuses on the effects of A-site substitution-induced octahedra distortions on the crystalline structure and microwave dielectric properties.

Recently, the concept of high-entropy ceramics (HECs) has rapidly evolved in the fields of metallic oxides, nitrides or carbides. The unique properties of HECs, such as high ionic conductivity [9], high dielectric constant [10], low thermal conductivity, and excellent thermal stability [11–12], have driven significant advancement in ceramic applications. In particular, high-entropy perovskite ceramics exhibit intriguing homogeneous single solid-solution phases [13]. Therefore, there is growing interest in exploring the phase structures, substitution mechanisms, and microwave dielectric properties of high-entropy perovskite ceramics. In this study, the effects of multi-element doping in CSZ ceramics would be discussed, including Ba and Mg doping. Previous

* Corresponding author.
E-mail address: yc56@mail.nsysu.edu.tw (Y.-C. Lee).
† These authors contributed equally to this work.

https://doi.org/10.1016/j.oceram.2025.100793
Received 4 February 2025; Received in revised form 16 April 2025; Accepted 2 May 2025
Available online 2 May 2025

studies have shown that the addition of Mg ions enhances the insulation resistivity of Zn–Nb–Ti ceramics due to the electrovalence compensation effect [14], which also reduces the sintering temperature from 1000 °C to 950 °C. It is well established that MgO as a sintering additive, lowers the sintering temperature by promoting grain boundary diffusion [15]. Atomistic simulation using classical pair potentials suggest that Mg dopants tend to substitute A site atoms in perovskite ABO_3 structured ceramics [16]. Therefore, this paper investigates the phase composition, microstructure and dielectric properties of $Mg_xCa_{0.6-x}Sr_{0.39}Ba_{0.01}ZrO_3$ ceramic, including the perspective of high entropy effects.

2. Materials and methods

$CaCO_3$(99.0 % purity, 0.5 μm), $SrCO_3$(99.5 % purity, 1 μm), $BaCO_3$(99.7 % purity, 0.19 μm), MgO (99.9 % purity, 0.31 μm), and ZrO_2 (99.9 % purity, 1.3 μm, supplied by Unique Enterprise Co. Ltd., Taiwan) commercial powders were weighed using a four digits libra, according to the molar ratio for $(Ca_{0.6}Sr_{0.39}Ba_{0.01})ZrO_3$ (denoted as CSBZ) and $(Mg_xCa_{0.6-x}Sr_{0.39}Ba_{0.01})ZrO_3$ (denoted as MCSBZ01, MCSBZ03, and MCSBZ05 for 1 %, 3 %, and 5 % MgO addition) ceramics. These powders were subjected to zirconia ball milling for 24 h with solvent and 1.5wt% dispersant (Dispex AA4040, Tye Han Trading Co. Ltd., Taiwan). Subsequently, the milled powders were poured out, dried, and calcined at 1200 °C for 4 hours. The resulting powders were then subjected to ball milling again and mixed with a binder (polyvinyl alcohol, PVA). A spray granulator (OM-1500A, Shang Hai Ou Meng Industrial Co., Ltd.) was used to process granulation. Approximately 0.5 g of powder was uniaxially pressed into disk-shaped pellets with a thickness of ~1 mm and a diameter of 11.9 mm using a tablet press. The pellets were subsequently sintered in a conventional furnace at temperatures ranging from 1200 °C to 1350 °C for a duration of 2 hours. The bulk density of the sintered samples was determined using the Archimedes method. Initially, the dry weight of each sample was measured in air. The sample was then immersed in water and subjected to ultrasonic agitation for 5 min to eliminate any trapped air bubbles. The suspended (wet) weight was subsequently measured using a suspension wire setup. The bulk density was calculated by dividing the dry weight by the difference between the dry and wet weights. For each composition, five sintered specimens were measured to obtain an average density value, and the corresponding standard deviations were used to represent the error bars. The crystallinity of sintered samples was measured using an X-ray diffractometer (XRD, Bruker D8 Advance) with monochromatic Cu-K_α radiation (λ = 1.540598 Å). A scanning electron microscope (SEM, JOEL–6700 F) equipped with an energy-dispersive spectroscopy (EDS) was used to analysis the microstructures. For cross-sectional structural analysis, TEM specimens were prepared using a dual-beam focused ion beam (FIB) system (Hitachi HR2000). Following FIB preparation, the specimens were examined using a field-emission TEM (Talos F200X G2, Instrument ID: EM025600) operated at an accelerating voltage of 200 kV. Silver pastes were printed on both sides of the ceramic pellets as the electrodes, dried at 130 °C for 10 mins for the dielectric measurements. Capacitance and dielectric loss were measured at 1 MHz and 8.9 GHz using a LCR meter (GWINSTEKG, LCR-8101 G). The temperature coefficient of capacitance (TCC) was measured using a HP 4284A LCR meter and a tunable temperature chamber (Espec SH-262) from −55 °C to 120 °C.

3. Results and discussion

Fig. 1 shows the XRD patterns of CSBZ and MCSBZ samples, calcined at 1200 °C for 4 hours, with varying MgO dopant levels (0 %, 1 %, 3 %, and 5 %). Phase analysis reveals that the MCSBZ samples predominantly exhibit a single-phase $Ca_{0.612}Sr_{0.388}ZrO_3$ structure, without secondary phases at 0 % and 1 % doping. The obvious diffraction peaks correspond to an orthorhombic perovskite structure (space group P_{mcn}), consistent with standard data (JCPD: 89–8016). The lattice constants for the CSZ

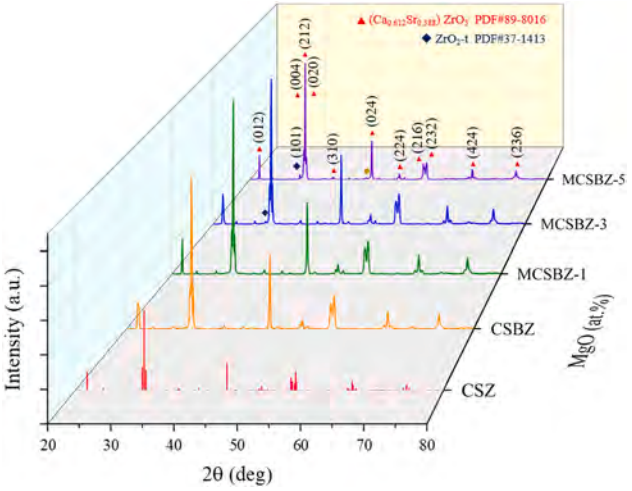

Fig. 1. XRD patterns of $(Ca_{0.6-x}Mg_xSr_{0.39}Ba_{0.01})ZrO_3$ powder calcined at 1200 °C for 4 h.

samples are a = 8.09460 Å, b = 5.67580 Å, c = 11.56740 Å [6]. However, MCSBZ-3 and MCSBZ-5 ceramics show weak secondary phase peaks at 30.09°, corresponding to a cubic ZrO_2 phase (JCPD: 49–1642). This secondary phase is attributed to ZrO_2 precipitation in CSZ ceramics, probably resulting from MgO substitution at the B site [17]. Except for the small amount of ZrO_2 present in the 3 % and 5 % MgO-doped samples, all calcinated samples remained mostly high-purity, single--phase CSZ, suitable for the sintering process.

Fig. 2 presents the bulk densities of MCSBZ ceramics sintered at temperatures ranging from 1200 °C to 1350 °C. Previous studies have shown that CSZ ceramics are typically sintered around 1490 °C [18,19] to achieve optimal densification and enhanced dielectric properties. The addition of Ba has been found to improve the bulk density of CSZ ceramics while lowering the required sintering temperature. A maximum bulk density of 4.7 g/cm^3 was recorded for the sample with 1 % Ba doping reaching 95 % of the theoretical density for $Ca_{0.612}Sr_{0.388}ZrO_3$ [6]. The trends in the curves suggest that both the MgO dopant and sintering temperature play a role in enhancing the bulk density of MCSBZ ceramics. Each MgO concentration corresponds to an optimal sintering temperature. At a fixed doping level, the apparent density increases with rising sintering temperature, eventually reaching the theoretical density of CSZ ceramic at the densification temperature.

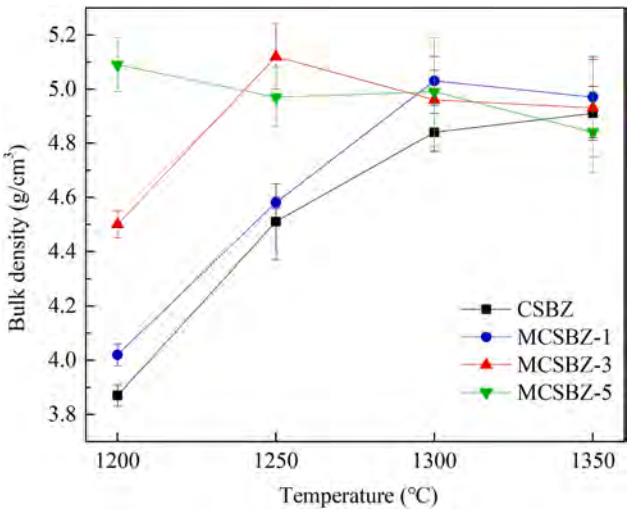

Fig. 2. Bulk density of $(Ca_{0.6-x}Mg_xSr_{0.39}Ba_{0.01})ZrO_3$ ceramics with different sintering temperatures.

Beyond this optimal temperature, a slight decrease in density is observed due to over-sintering [20]. Conversely, when sintering temperatures are held fixed, the density initially increases with MgO concentration, reaching a peak, followed by a slight decline, as illustrated in Fig. 2. The reduction in optimal sintering temperature due to doping elements is not unique to this study; similar trends have been observed in other systems, such as $Ce_2[Zr_{1-x}(Co_{1/2}W_{1/2})_x]_3(MoO_4)_9(CZ_{1-x}(CW)_xM)$ [21]. The maximum bulk densities for MCSBZ03 sintered at 1250 °C was recorded at 5.1 g/cm^3. Consequently, using MgO as a dopant proves beneficial in enhancing the bulk density of CSBZ ceramics while also lowering the required sintering temperatures.

The XRD patterns of $Mg_xCa_{0.6-x}Sr_{0.39}Ba_{0.01}ZrO_3$ (MCSBZ) series sintered at 1350 °C are shown in Fig. 3(a). The phase analysis reveals that MCSBZ samples consistently form a single phase $Ca_{0.612}Sr_{0.388}ZrO_3$ structure without detectable secondary phases at MgO concentrations of 0 % and 1 %. The high entropy $Mg_xCa_{0.6-x}Sr_{0.39}Ba_{0.01}ZrO_3$ ceramics exhibit a kaleidoscopic ability to maintain single-phase stability, even with diverse elemental compositions. This feature ensures consistent dielectric performance without phase segregation. However, as the MgO content increases to 3 %, a secondary ZrO_2 phase appears, resulting from Mg^{2+} substitution at the B-site of Zr^{4+} [18]. When the MgO content is further increased to 5 %, additional secondary phases are observed, such as the ZrO_2 (101) plane at 30.09° and the MgO (200) plane at 42.9°, as indicated in Fig. 3(a). The secondary phases in MCSBZ ceramics are thus linked to Mg^{2+} incorporation, where Mg^{2+} substitution in the perovskite structure leads to ZrO_2 precipitation in MCSBZ03. Additionally, excess MgO doping in MCSBZ05 not only induces the formation of ZrO_2 and MgO secondary phases but also triggers the formation of other unidentified secondary phases. The unidentified peaks at 32.9° and 33.4° are associated with Mg-rich phases, which will be further discussed in the EDS analysis. The insets in Fig. 3(a) provide a magnified view of the diffraction patterns from 31° to 31.5°, supporting this interpretation of Mg^{2+} substitution. When MgO doping is at 1 %, the enlarged view of the CSZ (212) plane shows the peak shift from 31.26° to 31.32 and decreases to 31.29° and 31.24° at 3 % and 5 % MgO doping, respectively. This indicates a relationship between Mg^{2+} substitution and the emergence of secondary phases. Fig. 3(b) presents the XRD patterns of MCSBZ01 samples sintered at different temperatures. All Mg-doped CSBZ ceramics exhibit a single phase $Ca_{0.612}Sr_{0.388}ZrO_3$ structure, confirming that 1 % Mg^{2+} is successfully incorporated into the CSZ ceramic lattice without generating secondary phase, even at elevated sintering temperatures, such as 1300 °C or 1350 °C.

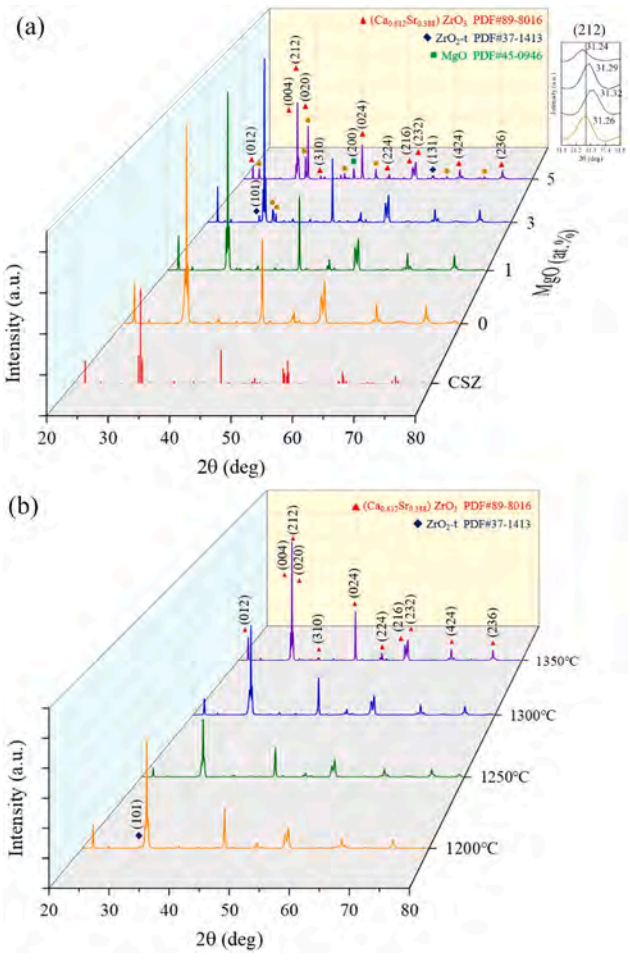

Fig. 3. (a)XRD patterns of $(Ca_{0.6-x}Mg_xSr_{0.39}Ba_{0.01})ZrO_3$ ceramics sintered at 1350 °C for 2 h. (b)XRD patterns of $(Ca_{0.59}Mg_{0.01}Sr_{0.39}Ba_{0.01})ZrO_3$ ceramics sintered at different temperatures.

Fig. 4 shows the lattice parameters of MCSBZ ceramics sintered at 1350 °C, which were calculated from the XRD patterns. The detailed values are systematic listed in Table 1. The lattice constants of the CSZ samples were calculated from the XRD peaks corresponding to the (hkl) planes using the reciprocal lattice vector relation:

$$\frac{1}{d^2_{(h,k,l)}} = \frac{h^2}{a^2} + \frac{k^2}{b^2} + \frac{l^2}{c^2}$$

Additionally, the crystallite size and full width at half maximum (FWHM) were estimated using the Scherrer equation:

$$d_{hkl} = \frac{k\lambda}{\beta\cos\theta}$$

The ionic radii of Mg^{2+} and Zr^{4+} are 72 pm, and 72 pm [22]. Compared to the larger ionic radii of Ca^{2+} (100 pm) and Sr^{2+} (144 pm) [6], the closer match in size allows Mg^{2+} to more easily replace Zr^{4+} at the B-site. However, the oxygen vacancies generated by Mg^{2+} incorporation would decrease lattice constant [23], leading to a decrease in the ***a***-axis and ***b***-axis. But an increase in the ***c***-axis as MgO doping rises from 0 % to 1 %, revealing an anisotropic strain in lattice structure. From 1 % to 5 % MgO doping, the lattice parameters exhibit the opposite trend, with an increase in the ***a***-axis and ***b***-axis, and a decrease in the ***c***-axis This is due to the solubility limit of Mg^{2+} substitution for Zr^{4+}. When the MgO content exceeds 1 %, the excess dopant cannot fully incorporate into the B-site, leading to reduced lattice deformation and the distortion of perovskite structure, the lattice arrangement returning to the structure seen in undoped samples (CSZ). These findings align with the density measurements results.

Fig. 5 shows SEM images illustrating the microstructure of MCSBZ01 ceramics sintered at 1350 °C with varying MgO doping levels. The surface morphologies of CSBZ, MCSBZ01, and MCSBZ03 display a dense, clear structure with low porosity appearance. The average grain sizes of CSBZ, MCSBZ01, MCSBZ03, and MCSBZ05 are 1.35, 1.48, 1.69 and 1.59

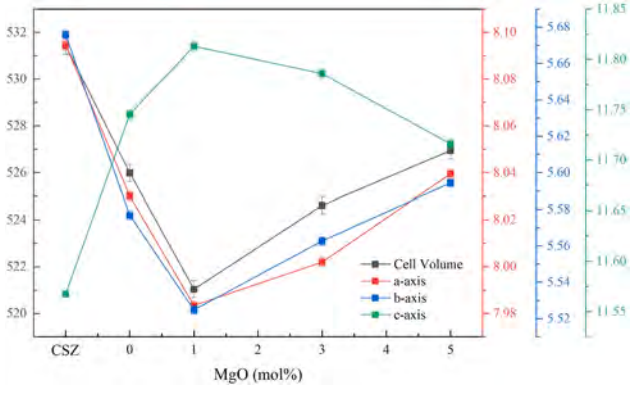

Fig. 4. The lattice parameters of $(Ca_{0.6-x}Mg_xSr_{0.39}Ba_{0.01})ZrO_3$ ceramics sintered at 1350 °C.

Table 1
Lattice parameters of (Ca,Mg,Sr,Ba)ZrO_3 ceramics sintered at 1350 °C.

$(Ca_{0.6-x}Mg_xSr_{0.39}Ba_{0.01})ZrO_3$	a(Å)	b(Å)	c(Å)	Volume (Å^3)	FWHM (°)
$x = 0$	8.030	5.577	11.745	525.99	0.145
$x = 0.01$	7.983	5.525	11.813	521.04	0.130
$x = 0.03$	8.002	5.563	11.786	524.62	0.100
$x = 0.05$	8.040	5.594	11.716	526.94	0.121

μm, respectively. The increase in grain size from 0 % to 3 % MgO doping is attributed to the sintering enhancement of MgO. On the contrary, the decrease in grain size from 3 % to 5 % MgO doping is attributed to the formation of secondary phase, including microstructural defects and flakes, become apparent on the MSCBZ05 sample. These microstructures are associated with the reduction in grain size [24]. This assumption can be confirmed by the EDS analysis results, detailed in Table 2. Elemental composition at point A in Fig. 5(d) shows O (38.3 %), Ca (13.9 %), Sr (10.2 %), Zr (37 %), Ba (0.42 %), and Mg (0.18 %). The ratios of Ca, Sr, Ba, Zr, and O are consistent with the atomic composition of $Ca_{0.6}Sr_{0.4-}Ba_{0.01}ZrO_3$, but the Mg content is only 0.18 %. In contrast, at point B and C, the Mg concentration increases to 5.13 % and 5.81 %, respectively, indicating a non-uniform distribution of Mg in the MCSBZ sample. These flakers are attributed to the Mg-rich secondary phase observed in the XRD patterns [25]. Besides, the reported uncertainty reflects estimated measurement error based on known instrumental and methodological limitations. Typical uncertainties are approximately ±2 at% for major elements (above 10 at%), ±3 at% for intermediate concentrations (1–10 at%), and up to ±5 at% for trace elements (below 1 at%) [26,27]. These estimated errors have now been indicated accordingly in Table 2. The high-entropy effect arises from an overall increase in the configurational disorder of the system. As the number of dopant species increases, the configurational entropy (ΔS_{conf}) also increases, thereby enhancing the system's thermodynamic stability. The configurational entropy of a solid solution can be estimated using the following expression:

$$\Delta Sconf = -R\sum_{i=1}^{n} x_i lnx_i$$

Where R is the gas constant (8.314 J/mol·K) and x_i is the atomic fraction of the i th element in the composition. In the $Mg_xCa_{0.612-x}Sr_{0.387}Ba_{0.001}ZrO_3$ system, when the Mg content increases from $x = 0$ to $x = 0.05$, the configurational entropy increases from 5.61 J/(mol·K) to 7.05 J/(mol·K), indicating a rise of approximately 1.44 J/(mol·K). This result confirms that greater compositional complexity leads to higher entropy, intensifying the high-entropy effect. For example, an increase in entropy can enhance the dielectric properties, a point that will be discussed in more detail later. However, the atomic solid solubility limit and lattice strain energy must also be taken into

Table 2
EDS analysis of $(Ca_{0.55}Mg_{0.05}Sr_{0.39}Ba_{0.01})ZrO_3$ ceramics sintered at 1350 °C.

	Element (At%)					
Position	O	Ca	Sr	Zr	Ba	Mg
A	38.3 %	13.9	10.2	37.0	0.42	0.18
B	53.8	15.1	4.6	20.8	0.59	5.13
C	59.5	14.4	2.99	17.0	0.24	5.81

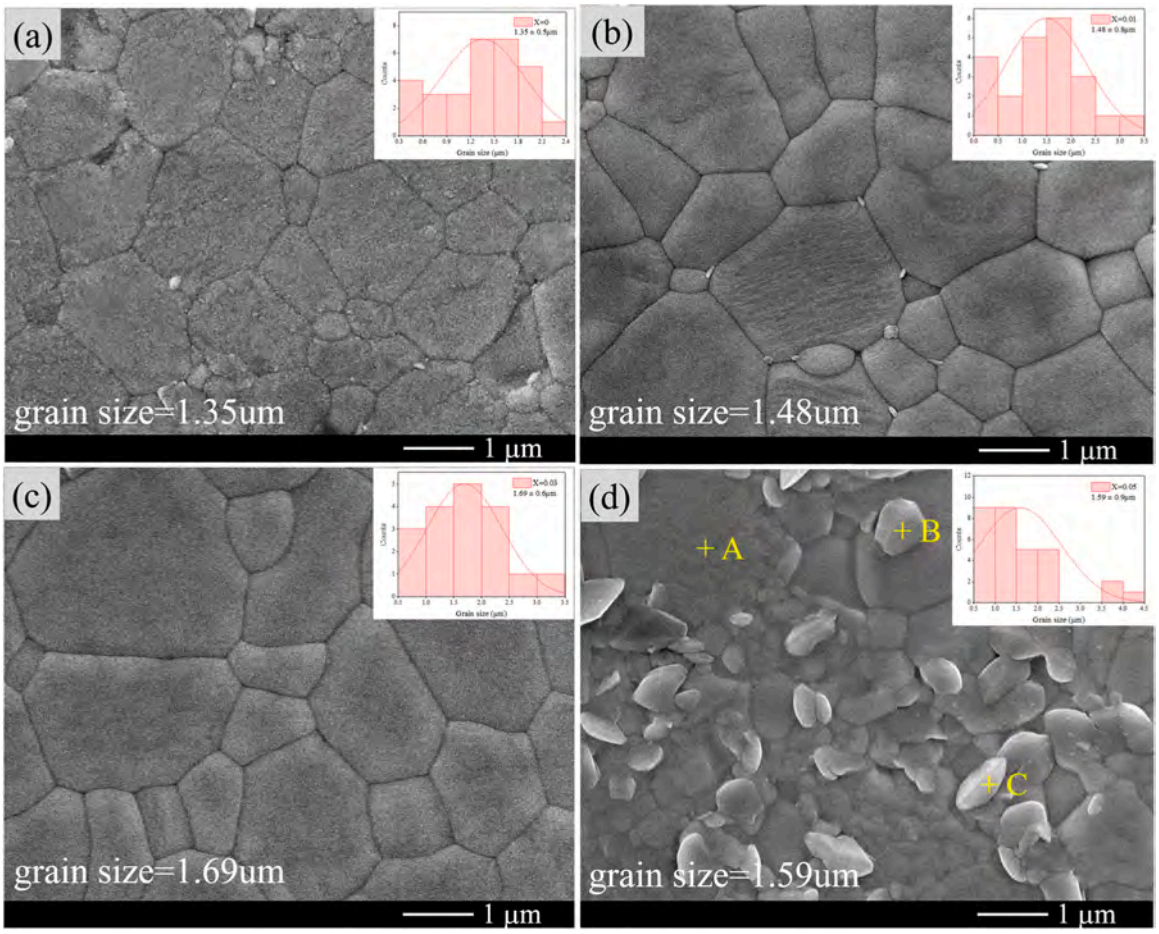

Fig. 5. SEM microstructure of $(Ca_{0.6-x}Mg_xSr_{0.39}Ba_{0.01})ZrO_3$ ceramics sintered at 1350 °C (a) $x = 0$, (b) $x = 0.01$, (c) $x = 0.03$, (d) $x = 0.05$. The insets indicate that grain size of $(Ca_{0.6-x}Mg_xSr_{0.39}Ba_{0.01})ZrO_3$ ceramics sintered at 1350 °C (a) $x = 0$, (b) $x = 0.01$, (c) $x = 0.03$, (d) $x = 0.05$.

consideration. According to the atomic solid solubility limit, an excessive amount of MgO incorporation induces high lattice strain energy, thereby promoting the formation of secondary phases [28]. This trend is further supported by the compositional analysis in Table 2, which shows that points B and C have higher concentrations of Mg, indicating the presence of a Mg-rich secondary phase. This phenomenon can also be found in the high entropy metal carbides series [29,30].

Fig. 6 presents TEM microstructural analysis of MCSBZ01 ceramics sintered at 1350 °C. Fig. 6(a) shows TEM bright field images of the specimens. Selected electron diffraction patterns were captured at triangular point A and grain B, in Fig. 6(b) and (c), respectively. The electron diffraction patterns and ***d***-spacing in both images confirm that both the grains A and B correspond to the $Ca_{0.612}Sr_{0.388}ZrO_3$ phase, with zone axes of [03$\underline{1}$] and [06$\underline{1}$], respectively. The EDS analysis, shown in Fig. 6(d), reveals atomic ratios close to the composition of $Ca_{0.612}Sr_{0.388}ZrO_3$ phase with ~1 % of Ba and Mg concentration. All grains in the MCSBZ01 sample exhibited the primary $Ca_{0.612}Sr_{0.388}ZrO_3$ phase, with no secondary phase detected.

This result aligns with the XRD and density measurements, confirming that 1 % MgO is the solubility limit for the $Ca_{0.612}Sr_{0.388}ZrO_3$ perovskite structure. Additionally, some dislocations were observed at the grain boundary between grains A and grain B, as shown in Fig. 6(e). Similar dislocations were commonly found elsewhere in the MCSBZ01 sample, as seen in Fig. 6(f). These dislocations are associated with oxygen vacancies generated by two different models. The schematic diagrams in Fig. 7 illustrate the details of B-site substitution, where Mg^{2+} or Ca^{2+} replaces the Zr^{4+} position, leading to the formation of oxygen vacancies. First one, due to similar ionic radii, oxygen vacancies are formed when Zr^{4+} is substituted by Mg^{2+} at the B-site. The defect equation can be represented by the following equation.

$$MgO \rightarrow Mg''_{Zr} + V_o^{\bullet\bullet} + Oo \quad (1)$$

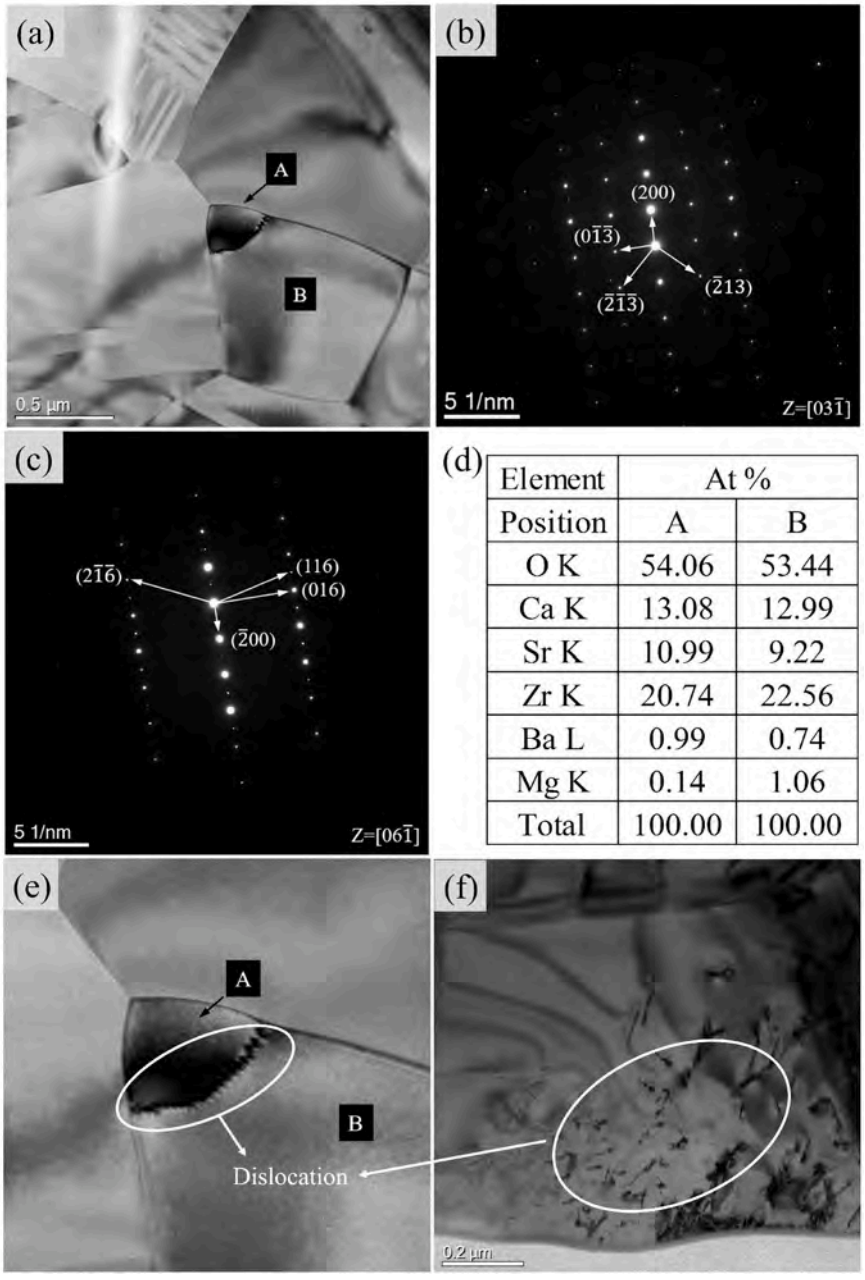

Element	At %	
Position	A	B
O K	54.06	53.44
Ca K	13.08	12.99
Sr K	10.99	9.22
Zr K	20.74	22.56
Ba L	0.99	0.74
Mg K	0.14	1.06
Total	100.00	100.00

Fig. 6. (a) TEM micrograph of sample $(Ca_{0.59}Mg_{0.01}Sr_{0.39}Ba_{0.01})ZrO_3$ ceramics sintered at 1350 °C, (b) diffraction pattern of position A, (c) diffraction pattern of position B, (d) elemental analysis of positions A and B, (e) and (f) TEM micrograph of sample $(Ca_{0.59}Mg_{0.01}Sr_{0.39}Ba_{0.01})ZrO_3$ with enlargement magnification.

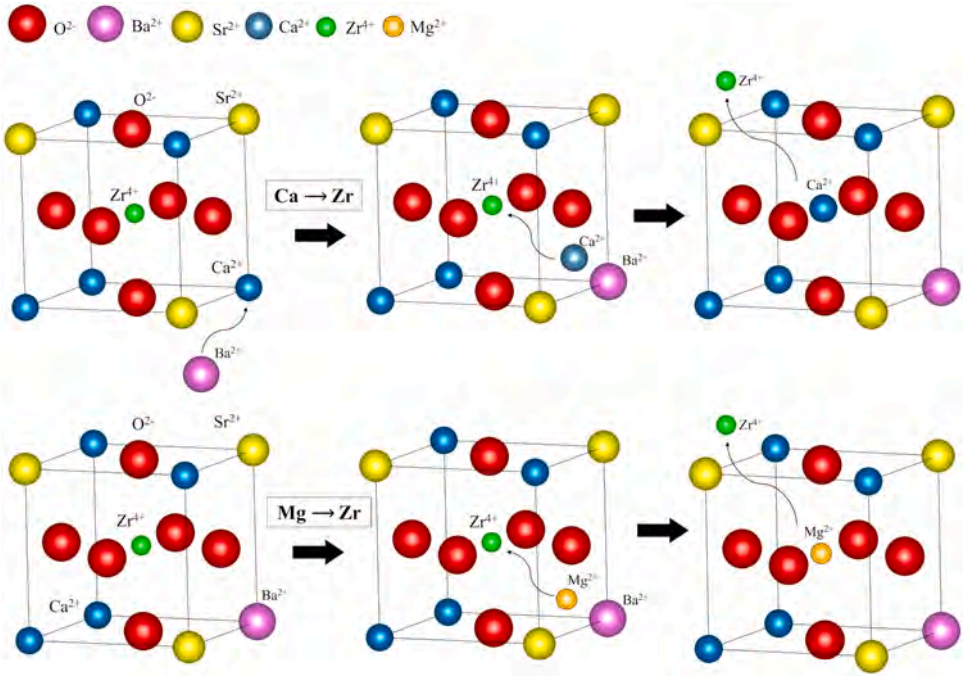

Fig. 7. Mechanism of B-site substitution between Ca^{2+} and Mg^{2+} and the formation of oxygen vacancy.

These oxygen vacancies are likely to contribute to increased dislocation within the structure. The concentration of oxygen vacancies and dislocations is expected to peak at 1 % MgO doping, as this represents the solubility limit of MgO in CSBZ ceramics. On the other hand, excessive Ca^{2+} may occupy the Zr^{4+} position at the B site [31,32]. When Ba^{2+} substitutes the Ca^{2+} cations on the A site, the displaced Ca^{2+} cations would move to occupy the B site, leading to more oxygen vacancies [6]. The defect equation can be represented by the following equations:

$$BaO + Ca_{Ca} \rightarrow Ba_{Ca} + CaO \quad (2)$$

$$CaO \rightarrow Ca''_{Zr} + V_o^{\bullet\bullet} + Oo \quad (3)$$

Fig. 8 presents EDS mapping and elemental composition of the MCSBZ03 sample. At least three distinct grains are visible in the STEM image in Fig. 8(a), labeled as grains A, B, and C. Fig. 8(b) through 8(h) display the elemental distributions of Mg, O, Ba, Ca, Sr, and Zr. It is evident that Mg and O are concentrated in grain B, while Ba, Ca, Sr, and Zr are absent from this region. This observation is consistent with the SEM, XRD and EDS analyses, which show Mg-rich phases in the MCSBZ03 and MCSBZ05 samples. Since the MgO content in these

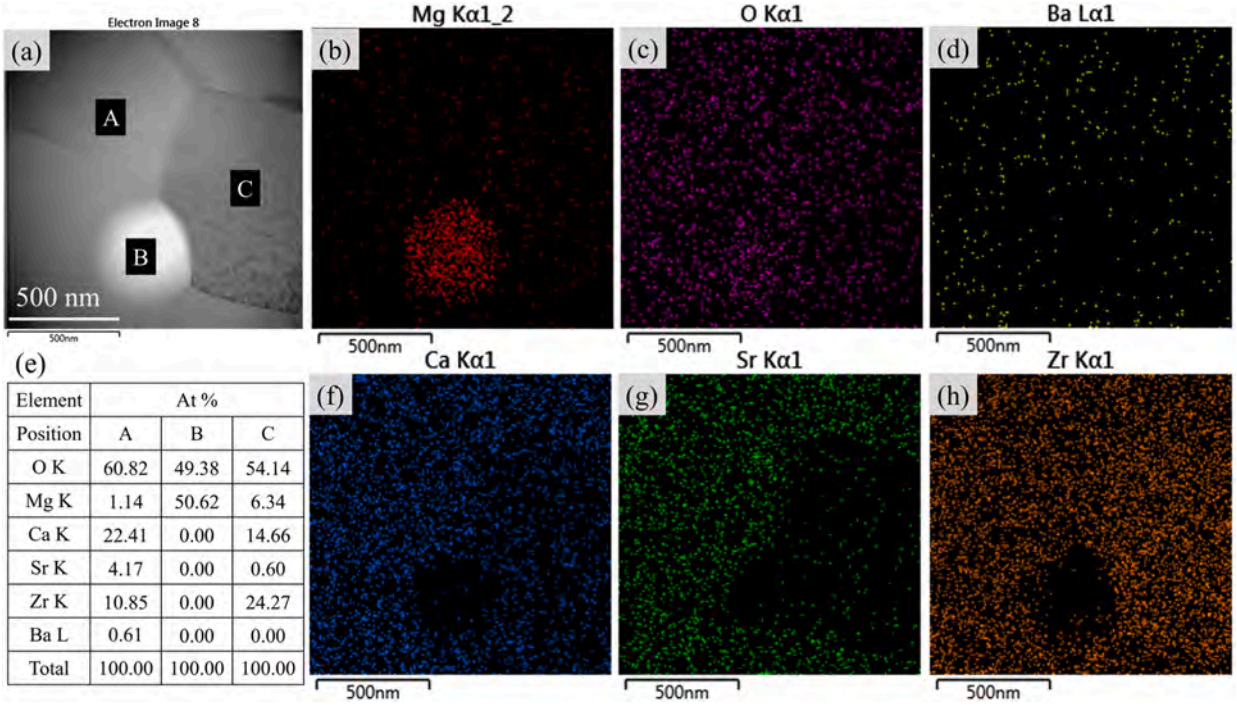

Element	At %		
Position	A	B	C
O K	60.82	49.38	54.14
Mg K	1.14	50.62	6.34
Ca K	22.41	0.00	14.66
Sr K	4.17	0.00	0.60
Zr K	10.85	0.00	24.27
Ba L	0.61	0.00	0.00
Total	100.00	100.00	100.00

Fig. 8. Elemental analysis of sample $(Ca_{0.57}Mg_{0.03}Sr_{0.39}Ba_{0.01})ZrO_3$ ceramics sintered at 1350 °C.

samples exceeds the solubility limit at 3 % and 5 %, the excess Mg leads to the formation of Mg-rich secondary phases, as confirmed by the XRD, EDS and TEM results.

The dielectric properties of MCSBZ ceramics as a function of MgO addition were measured at 1 MHz, as shown in Fig. 9. The trend of the dielectric constants with respect to sintering temperature closely follows the trend of bulk density (Fig. 4), as grain size directly impacts the dielectric constant. As the sintering temperature increases, the density of MCSBZ ceramics rises significantly, leading to enhanced dielectric constant (ε_r) values of the CSBZ01 ceramics, increasing from 19.7 at 1350 °C to 33.0 at 1450 °C. Since MgO affects grain growth in MCSBZ ceramics, the dielectric constant is closely associated with MgO content. Notably, ε_r values increase with MgO doping from 0 % to 1 % across all sintering temperatures (1200 to 1350 °C). However, beyond 1 % MgO doping, the ε_r trend diverges. At lower sintering temperatures (1200 °C and 1250 °C), the permittivity of MCSBZ continues to rise with increasing MgO content. This is likely due to the sintering enhancement effect of MgO doped, which promotes grain and grain boundary diffusion, thereby increasing both density and ε_r values [33,34]. This is supported by the SEM images, which show that average grain size increases with MgO composition. On the other hand, once the bulk density reaches its saturation point, further MgO addition leads to the precipitation of excess MgO, causing a slight decrease in density. As a result, ε_r values decrease with MgO doping from 1 % to 5 % at sintering temperatures of 1300 °C and 1350 °C. This decrease is accompanied by the formation of Mg-rich secondary phase, as observed in XRD, SEM, and TEM analyses.

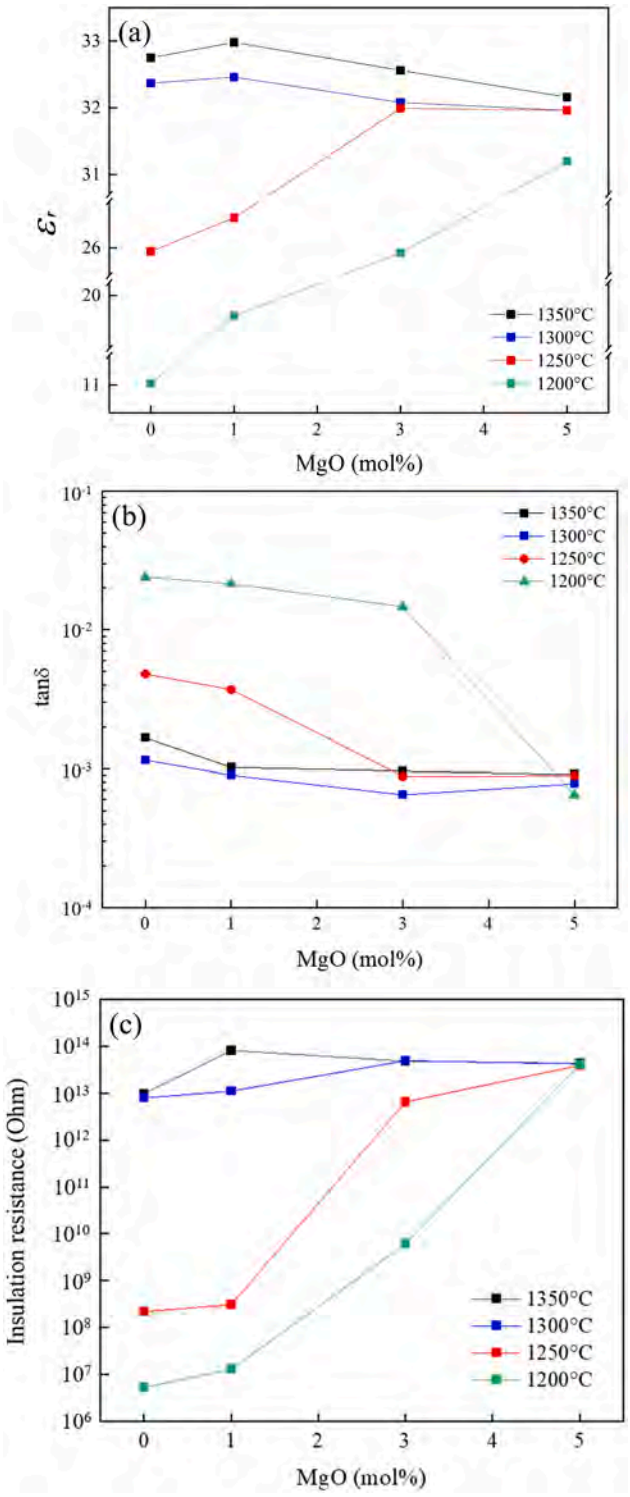

Fig. 9. Different sintering temperature of (a) dielectric constants (b) dielectric loss (c) insulation resistance of $(Ca_{0.6-x}Mg_xSr_{0.39}Ba_{0.01})ZrO_3$ ceramics measured at 25 °C, 1 MHz.

As shown in Fig. 9(b), the dielectric loss decreases with increasing sintering temperatures, reaching a minimum at 1300 °C. It is well known that oxygen vacancies and other defects contribute to increased dielectric losses [35]. This suggests that denser sintering at higher temperatures or the addition of sintering aids can significantly reduce oxygen vacancies and other defects [36]. The MCSBZ ceramics consistently exhibit lower dielectric loss compared to CSBZ ceramics at all sintering temperatures. For example, when comparing CSBZ, MCSBZ01 and MCSBZ03 ceramics sintered at 1250 °C, the dielectric loss shows a sharp reduction, from 48.0 × 10^{-3} to 8.8 × 10^{-3}. This demonstrates that MgO doping effectively improves the sintering performance of MCSBZ ceramics. Moreover, dielectric loss remains low with increasing MgO content across all sintering temperature. This is attributed to the verdant complexity of high-entropy systems hinders charge mobility, effectively suppressing leakage currents and dielectric loss. The mosaic of elements creates a labyrinthine network that limits carrier movement. Fig. 9(c) shows the insulation resistance of MCSBZ ceramics, which follow similar trends as the density measurements. Improved sintering conditions directly enhance insulation resistance, with the highest value measured for MCSBZ01 sintered at 1350 °C, yielding 4.3 × 10^{14} Ω. All the dielectric results are systemically summarized in Table 3. The high entropy ceramics intertwine multiple cations with varying valence states and ionic radii, creating a labyrinth of charge distribution. This intricate charge balance mitigates localized electric field distortions, enabling greater stability and reducing leakage currents [37].

Table 4 presents the dielectric properties of MCSBZ ceramics sintered at 1350 °C and measured at high frequencies (8.9 GHz). Typically, permittivity usually decreases with increasing frequency due to reduced interfacial polarization in ordinary dielectric materials [38]. However, the dielectric constant and dielectric loss of all MCSBZ ceramics show only slight deviations under microwave conditions compared to the CSZ ceramics. This stability is attributed to the more uniform ionic distribution, allowing polarization to resonate more effectively at higher frequencies [39]. These findings highlight the potential of MCSBZ ceramics for high-frequency applications. The Qf values, calculated and shown in Fig. 10, exhibit a relationship with several factors. First, bulk density is directly proportional to Qf since lower bulk density typically results in more pores and defects, which increase energy loss and interfacial polarization during electric field switching. The bulk density rises initially at 1 % MgO doping and declines at 3 % to 5 %, mirroring the Qf trends. Besides, the presence of secondary phases in MCSBZ03 and MCSBZ05 also contributes to reduced Qf values. Second, the atomic packing fraction (APF), which represents the packing density of atoms in the crystal structure, influences the Qf values and can be expressed by the following formula [40]:

Table 3
Dielectric properties and bulk density of $(Ca_{0.6-x}Mg_xSr_{0.39}Ba_{0.01})ZrO_3$ ceramics sintered at different temperatures.

Sintering Temperature (°C)	$(Ca_{0.6-x}Mg_xSr_{0.39}Ba_{0.01})ZrO_3$	Bulk Density (g/cm^3)	Permittivity < 1 MHz >	Dielectric Loss (tanδ × 10^{-4})	Insulation Resistance(Ω)
1350	$X = 0$	4.91	32.75	16.6	9.8×10^{12}
	$X = 0.01$	4.97	32.98	10.2	6.1×10^{13}
	$X = 0.03$	4.93	32.56	9.6	4.7×10^{13}
	$X = 0.05$	4.84	32.16	9.1	4.3×10^{14}
1300	$X = 0$	4.84	32.37	11.5	7.9×10^{12}
	$X = 0.01$	5.03	32.46	9.0	1.1×10^{13}
	$X = 0.03$	4.96	32.08	6.5	4.9×10^{13}
	$X = 0.05$	4.99	31.96	7.8	3.2×10^{13}
1250	$X = 0$	4.51	25.92	48	2.2×10^{8}
	$X = 0.01$	4.58	26.65	37	3.1×10^{8}
	$X = 0.03$	5.12	31.99	8.8	6.5×10^{12}
	$X = 0.05$	4.97	31.96	8.9	3.9×10^{13}
1200	$X = 0$	3.87	11.03	240	5.3×10^{6}
	$X = 0.01$	4.02	19.69	215	1.3×10^{7}
	$X = 0.03$	4.50	25.89	147	6.1×10^{9}
	$X = 0.05$	5.09	31.20	6.5	4.1×10^{13}

Table 4
Dielectric properties measured at high frequencies of $(Ca_{0.6-x}Mg_xSr_{0.39}Ba_{0.01})ZrO_3$ ceramics sintered at 1350 °C.

$(Mg_xCa_{0.6-x}Sr_{0.39}Ba_{0.01})ZrO_3$	Permittivity (1 MHz)	Permittivity (8.9 GHz)	Dielectric Loss (tanδ*10^{-4})	$Q \times f$ (GHz)	τ_f (ppm/°C)
$(Ca_{0.6}Sr_{0.4})ZrO_3$–1500 °C	28.08	24.29	8.5	12,470	41.8
$X = 0$	32.75	31.27	4.0	21,708	−66.8
$X = 0.01$	32.98	31.48	4.0	22,012	−54.4
$X = 0.03$	32.56	30.99	4.6	18,888	−33.5
$X = 0.05$	32.16	30.28	6.4	13,971	52.8

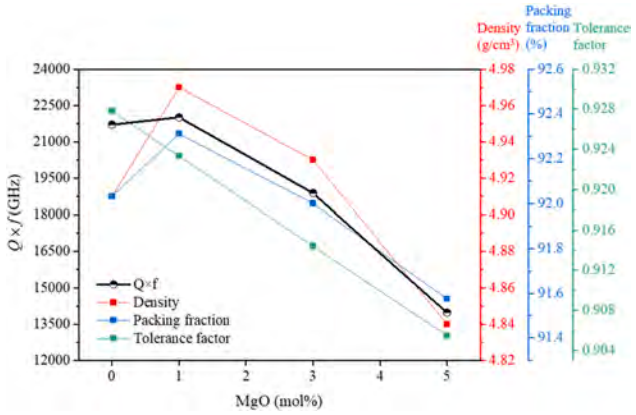

Fig. 10. Quality factor, density, packing fraction and tolerance factor of $(Ca_{0.6-x}Mg_xSr_{0.39}Ba_{0.01})ZrO_3$ ceramics with different MgO content sintered at 1350 °C.

$$APF = \frac{N_{atoms}\ V_{atom}}{V_{crystal}}$$

The parameter $\boldsymbol{N_{atoms}}$ represents the number of atoms in the primitive cell, while $\boldsymbol{V_{atom}}$ and $\boldsymbol{V_{crystal}}$ denote the volume of atoms and the volume of the crystal, respectively. According to the XRD measurements, the crystal volume $\boldsymbol{V_{crystal}}$ for CSBZ, MCSBZ01, MCSBZ 03, and MCSBZ 05 were calculated to be 92.03 %, 92.31 %, 92 %, and 91.58 %, respectively. These values align well with the trends in Qf values. Another significant parameter for predicting the stability of the perovskite structure is the Goldschmidt tolerance factor $\boldsymbol{t}$, calculated using the formula:

$$t = \frac{r_A + r_X}{\sqrt{2}(r_B + r_X)}$$

where r_A, r_B, and r_X are the ionic radii of the A, B, and X ions, respectively. C.J. Bartel et al. developed a refined method for predicting the stability of the perovskite structure by incorporating the oxidation state of the ABX_3 structure [41,42]. For $Ca_{0.6}Sr_{0.4}ZrO_3$, the tolerance factor calculation is simplified due to the equal oxidation state [43,44]. J. Joseph et al. [45] reported a tolerance factor of 0.924 for $Ca_{0.6}Sr_{0.4}ZrO_3$, compared to 0.965 for $SrZrO_3$, reflecting the looser packing of $Ca_{0.6}Sr_{0.4}ZrO_3$ relative to $SrZrO_3$. A. M. Glazer identified three key factors contributing to the stability of the perovskite structure: tilting of the anion octahedra, cation displacements, and octahedra distortions [46,47]. The tolerance factors of CSBZ, MCSBZ01, MCSBZ03, and MCSBZ05 were calculated as 0.928, 0.923, 0.914, and 0.905, respectively. This decreasing trend in tolerance factor highlights the increasing difficulty of incorporating higher amounts of Mg cations, which correlates with the marked decrease in Qf values at 3 % and 5 % MgO doping.

In Fig. 11, we compare dielectric constant and Qf values of CSZ, CSBZ, and MCSBZ samples. It is evident that dielectric properties are enhanced with the introduction of Ba and Mg cations incorporation. Specifically, MgO doping in MCSBZ01 improves both the dielectric

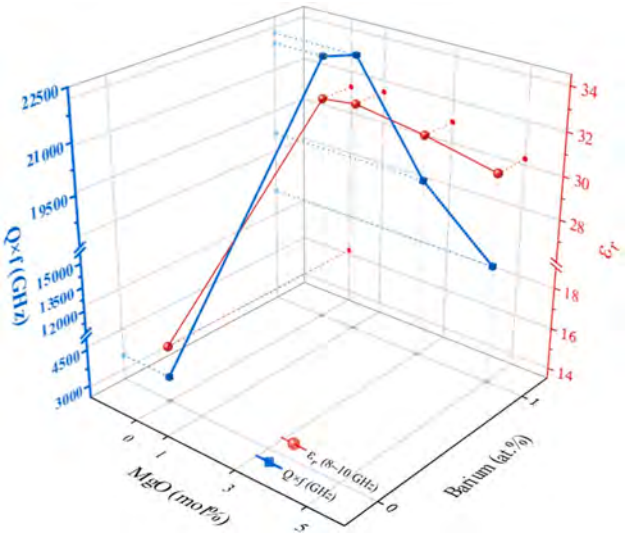

Fig. 11. The quality factor and the dielectric constants of $(Ca_{0.6-x}Mg_xSr_{0.39}Ba_{0.01})ZrO_3$ ceramics sintered at 1350 °C as a function of different MgO and Barium content.

constant and Qf values compared to CSBZ. Additionally, the τ_f values improve from −66.8 ppm/ °C to −54.4 ppm/ °C, indicating that MCSBZ exhibit better thermal stability. Consequently, MCSBZ ceramic exhibited superior dielectric constants and Qf values compared to CSZ ceramics. These properties remain stable even as the measuring frequency increases to 8.9 GHz, owing to the stable structure of the material. Furthermore, a comparison between CSBZ sintered at 1350 °C and MCSBZ03 sintered at 1250 °C in Table 3 reveals that MgO doping enhances bulk density, dielectric constant, and reduces dielectric loss at low to medium frequencies. This demonstrates MgO's effectiveness as a sintering aid, lowing the required sintering temperature.

4. Conclusion

$Mg_xCa_{0.6}Sr_{0.4-x}Ba_{0.01}ZrO_3$ (x = 0.01, 0.03, and 0.05) ceramics were synthesized using the solid-state method. Mg incorporation notably enhances sintering condition, increasing the bulk density of the ceramics and reducing the sintering temperature, which is evident in the optimized properties of samples doped with 1 % Mg. We explore the crystalline structure and microwave dielectric properties of perovskite ceramics, focusing on B-site substitution, where Mg replaces Zr. The results of XRD confirm the formation of the primary phase, $Ca_{0.612}Sr_{0.388}ZrO_3$ across the entire range of Mg concentrations (x = 0.01 to 0.05). Mg doping in MCSBZ ceramics primarily maintains the perovskite structure $Ca_{0.612}Sr_{0.388}ZrO_3$ without secondary phase formation at lower doping levels. As Mg content increases to 3 % and 5 %, secondary phases like ZrO_2 and MgO precipitate due to the limited solubility of Mg in the lattice. However, the present of secondary phase confirmed that Mg substituted the ions at B site (Zr^{4+}) rather than A site, generating oxygen vacancies. The oxygen vacancies play a role in sintering enhancement, causing gradual lattice shrinkage and anisotropic strain in the MCSBZ ceramics. The results lead to a significant increase in bulk density and a reduction in sintering temperature. Among the compositions studied, MCSBZ ceramics with 1 % Mg doping (solubility limit) showed the best dielectric properties, with a permittivity of 32.98, dielectric loss of 10.2×10^{-4} and a high Q factor of 22,012 at 8–10 GHz. This substitution strategy proves to be an effective approach to improve the microwave dielectric properties of $Ca_{0.6}Sr_{0.4}ZrO_3$ ceramics, making them highly suitable for microwave device applications.

Funding

This work was supported by the National Science and Technology Council (NSTC), Taiwan through grant number MOST 111-2221-E-110-064-MY3 and NSTC 113-2221-E-110-015-MY3.

CRediT authorship contribution statement

Huei-Jyun Shih: Writing – review & editing, Writing – original draft, Investigation, Formal analysis. **Chin-Tung Shih:** Methodology, Investigation, Formal analysis, Data curation. **Ying-Chieh Lee:** Supervision, Resources, Project administration, Conceptualization.

Declaration of competing interest

The authors declare that they have no known competing financial interests or personal relationships that could have appeared to influence the work reported in this paper.

Acknowledgements

The authors would like to thank Dr. Hui-Chun Huang and Dr. Cheng-Da Tsai for their assistance at the Joint Center for High Valued Instruments, National Sun Yet-Sen University.

References

[1] W. Lou, M. Mao, K. Song, K. Xu, B. Liu, W. Li, I.M. Reaney, Low permittivity cordierite-based microwave dielectric ceramics for 5G/6G telecommunications, J. Eur. Ceram. Soc. 42 (6) (2022) 2820–2826.
[2] S. Wang, W. Luo, L. Li, M. Du, J. Qiao, Improved tri-layer microwave dielectric ceramic for 5 G applications, J. Eur. Ceram. Soc. 41 (1) (2021) 418–423.
[3] B. Ullah, M. Appiah, Y. Xiao, Y. Yang, D.Q. Tan, Optimizing microwave dielectric properties of low-temperature sintered Sr/Zn-substituted BaMg2V2O8 by mixing with TiO2, J. Am. Ceram. Soc. 107 (11) (2024) 7470–7484.
[4] C. A. Randall, H. Nishiyama, H. Shimizu, Impact of volatility, non-stoichiometry, and atmospheres in perovskite piezoelectric and dielectric materials J. Am. Ceram. Soc. 107 (12) (2024) 7921–7938.
[5] K. Nadaud, C. Borderon, R. Gillard, E. Fourn, R. Renoud, H.W. Gundel, Temperature stable $BaSrTiO_3$ thin films suitable for microwave applications, Thin. Solid. Films. 591 (2015) 90–96.
[6] Y.C. Lee, H.J. Shih, T.Y. Wang, C. Pithan, Effect of Ba addition on the dielectric properties and microstructure of $(Ca_{0.6}Sr_{0.4})ZrO_3$, J. Eur. Ceram. Soc. 44 (10) (2024) 5659–5667.
[7] T. Yamaguchi, Y. Komatsu, T. Otobe, Y. Murakami, Newly developed ternary (Ca, Sr, Ba) zirconate ceramic system for microwave resonators, Ferroelectrics. 27 (1) (1980) 273–276.
[8] S. Qiu, M. Li, G. Shao, H. Wang, J. Zhu, W. Liu, R. Zhang, (Ca, Sr, Ba) ZrO_3: a promising entropy-stabilized ceramic for titanium alloys smelting, J. Mater. Sci. Technol. 65 (2021) 82–88.
[9] D. Bérardan, S. Franger, A.K. Meena, N. Dragoe, Room temperature lithium superionic conductivity in high entropy oxides, J. Mater. Chem. A 4 (24) (2016) 9536–9541.
[10] B. Yang, Y. Zhang, H. Pan, W. Si, Q. Zhang, Z. Shen, Y.H. Lin, High-entropy enhanced capacitive energy storage, Nat. Mater. 21 (9) (2022) 1074–1080.
[11] Y. Pu, Q. Zhang, R. Li, M. Chen, X. Du, S. Zhou, Dielectric properties and electrocaloric effect of high-entropy $(Na_{0.2}Bi_{0.2}Ba_{0.2}Sr_{0.2}Ca_{0.2})TiO_3$ ceramic, Appl. Phys. Lett. (22) (2019) 115.
[12] S. Zhou, Y. Pu, Q. Zhang, R. Shi, X. Guo, W. Wang, T. Ouyang, Microstructure and dielectric properties of high entropy $Ba(Zr_{0.2}Ti_{0.2}Sn_{0.2}Hf_{0.2}Me_{0.2})O_3$ perovskite oxides, Ceram. Int. 46 (6) (2020) 7430–7437.
[13] S. Jiang, T. Hu, J. Gild, N. Zhou, J. Nie, M. Qin, J. Luo, A new class of high-entropy perovskite oxides, Scr. Mater. 142 (2018) 116–120.
[14] W. Sp, L. Jh, Mg-substituted $ZnNb_2O_6$–TiO_2 composite ceramics for RF/microwaves ceramic capacitors, J. Alloys. Compd. 509 (31) (2011) 8126–8129.
[15] K. Dai, R. Ma, X. Wang, Z. Zheng, Y. Fan, X. Zhao, X. Cao, Quantifying the improvement in dielectric properties of $BaSrTiO_3$-based ceramics by adding MgO, Materials. (Basel) 15 (8) (2022) 2875.
[16] N. Kuganathan, P. Iyngaran, R. Vovk, A. Chroneos, Defects, dopants and Mg diffusion in $MgTiO_3$, Sci. Rep. 9 (1) (2019) 4394.
[17] M. Zhang, J. Zhai, B. Shen, X. Yao, MgO doping effects on dielectric properties of $Ba_{0.55}Sr_{0.45}TiO_3$ ceramics, J. Am. Ceram. Soc. 94 (11) (2011) 3883–3888.
[18] L. Yang, Y. Liu, W. Zhang, G. Zhou, D. Jiang, H. Chen, B. Liu, High-temperature mechanical and thermal properties of $Ca_{1-x}Sr_xZrO_3$ solid solutions, J. Am. Ceram. Soc. 103 (3) (2020) 1992–2000.
[19] J.M.C. Yu-De Li, Y.C Lee, Dielectric properties and microstructures of $(Ca_xSr_{1-x})ZrO_3$ ceramics, J. Ceram. Process. Res. 19 (6) (2018) 461–466.
[20] H.J. Shih, Y.C. Lee, C.T. Yang, Effect of Nb_2O_5 doping on low-temperature sintering of TiO_2-Al_2O_3 ceramics, Open Ceramics 19 (2024) 100635.
[21] J. Bao, Y. Zhang, H. Wu, Y. Zhou, Z. Yue, Sintering characteristics, crystal structure and dielectric properties of cobalt-tungsten doped molybdate-based ceramics at microwave frequency, J Materiomics. 8 (5) (2022) 949–957.
[22] R. Rodríguez-Guzmán, P. Sarriguren, L.M. Robledo, S. Perez-Martin, Charge radii and structural evolution in Sr, Zr, and Mo isotopes, Phys. Lett. B 691 (4) (2010) 202–207.
[23] Y. Liu, B. Liu, H. Xiang, Y. Zhou, H. Nian, H. Chen, Y. Gao, Theoretical investigation of anisotropic mechanical and thermal properties of ABO_3 (A= Sr, Ba; B= Ti, Zr, Hf) perovskites, J. Am. Ceram. Soc. 101 (8) (2018) 3527–3540.
[24] H.J. Shih, Y.C. Lee, J.R. Pan, C. Chung, Effects of Sn addition in W-doped Ag paste against electrochemical corrosion and sulfurization, Anti-Corros. Methods Mater. (2024).
[25] N. Mansard, H. Stünitz, H. Raimbourg, J. Précigout, A. Plunder, L. Nègre, Relationship between microstructures and resistance in mafic assemblages that deform and transform, Solid Earth 11 (6) (2020) 2141–2167.
[26] D.E. Newbury, N.W. Ritchie, Is scanning electron microscopy/energy dispersive X-ray spectrometry (SEM/EDS) quantitative? Scanning 35 (3) (2013) 141–168.
[27] H.J. Shih, I. Lo, Y.C. Wang, C.D. Tsai, Y.C. Lin, Y.Y. Lu, H.C. Huang, Growth and characterization of GaN/In x Ga1− x N/In y Al1− y N quantum wells by plasma-assisted molecular beam epitaxy, Crystals. (Basel) 12 (3) (2022) 417.
[28] T. Schwab, K. Aicher, H. Razouq, G.A. Zickler, O. Diwald, Segregation engineering in MgO nanoparticle-derived ceramics: the impact of calcium and barium admixtures on the microstructure and light emission properties, ACS. Appl. Mater. Interfaces. 13 (21) (2021) 25493–25502.
[29] S.M. Smith II, W.G. Fahrenholtz, G.E. Hilmas, S. Curtarolo, Thermodynamic analysis of metal segregation in dual phase high entropy ceramics, J Materiomics. 10 (4) (2024) 889–895.
[30] F.Z. Dai, B. Wen, Y. Sun, Y. Ren, H. Xiang, Y. Zhou, Grain boundary segregation induced strong UHTCs at elevated temperatures: a universal mechanism from conventional UHTCs to high entropy UHTCs, J. Mater. Sci. Technol. 123 (2022) 26–33.

[31] N. Pisitpipathsin, P. Kantha, K. Pengpat, G. Rujijanagul, Influence of Ca substitution on microstructure and electrical properties of Ba (Zr, Ti) O3 ceramics, Ceram. Int. 39 (2013) S35–S39.
[32] D. Lin, Z. Ling, Effect of titanium substitution for zirconium on dielectric properties of (Ca0.45Sr0.55) ZrO3 ceramics, J. Chin. Ceram. Soc. 42 (7) (2014) 821–825.
[33] L. Li, M. Wang, Y. Liu, J. Chen, N. Zhang, Decisive role of MgO addition in the ultra-broad temperature stability of multicomponent $BaTiO_3$-based ceramics, Ceram. Int. 40 (1) (2014) 1105–1110.
[34] J.Y. Chen, C.L. Huang, A new low-loss microwave dielectric using $(Ca_{0.8}Sr_{0.2})TiO_3$-doped $MgTiO_3$ ceramics, Mater. Lett. 64 (23) (2010) 2585–2588.
[35] C. Pithan, H.Y. Lee, M.Y. Yeh, Y.C. Lee, D.F. Hennings, Microstructural and dielectric properties of $Ba_{0.45}Mg_{0.05}Sr_{0.5-x}CaxTiO_3$ high entropy ceramics, Mater. Chem. Phys. 296 (2023) 127290.
[36] M. Zhang, J. Zhai, B. Shen, X. Yao, MgO doping effects on dielectric properties of $Ba_{0.55}Sr_{0.45}TiO_3$ ceramics, J. Am. Ceram. Soc. 94 (11) (2011) 3883–3888.
[37] M. Zhang, S. Lan, B.B. Yang, H. Pan, Y.Q. Liu, Q.H. Zhang, Y.H. Lin, Ultrahigh energy storage in high-entropy ceramic capacitors with polymorphic relaxor phase, Science (1979) 384 (6692) (2024) 185–189.
[38] G. Zhang, D. Brannum, D. Dong, L. Tang, E. Allahyarov, S. Tang, L. Zhu, Interfacial polarization-induced loss mechanisms in polypropylene/$BaTiO_3$ nanocomposite dielectrics, Chem. Mater. 28 (13) (2016) 4646–4660.
[39] H.S. Park, K.H. Yoon, E.S. Kim, Relationship between the bond valence and the temperature coefficient of the resonant frequency in the complex perovskite $(Pb1-xCax)[Fe_{0.5}(Nb_{1-y}Ta_y)_{0.5}]O_3$, J. Am. Ceram. Soc. 84 (1) (2001) 99–103.
[40] Q. Sun, W.J. Yin, Thermodynamic stability trend of cubic perovskites, J. Am. Chem. Soc. 139 (42) (2017) 14905–14908.
[41] C.J. Bartel, C. Sutton, B.R. Goldsmith, R. Ouyang, C.B. Musgrave, L.M. Ghiringhelli, M. Scheffler, New tolerance factor to predict the stability of perovskite oxides and halides, Sci. Adv. 5 (2) (2019) eaav0693.
[42] T. Sato, S. Takagi, S. Deledda, B.C. Hauback, S.I. Orimo, Extending the applicability of the goldschmidt tolerance factor to arbitrary ionic compounds, Sci. Rep. 6 (1) (2016) 23592.
[43] M. Tarrida, H. Larguem, M. Madon, Structural investigations of $(Ca,Sr)ZrO_3$ and $Ca(Sn, Zr)O_3$ perovskite compounds, Phys. Chem. Miner. 36 (2009) 403–413.
[44] N.F. Muhamad, R.A.M. Osman, M.S. Idris, M.N.M. Yasin, Physical and electrical properties of $SrTiO_3$ and $SrZrO_3$, in: EPJ Web of Conferences 162, EDP Sciences, 2017 01052.
[45] J. Joseph, V. Sivasubramaniam, T.M. Vimala, V.R.K. Murthy, Structural study on Ca0. 6Sr0. 4ZrO3, Jpn. J. Appl. Phys. 38 (2R) (1999) 822.
[46] P.M. Woodward, Octahedral tilting in perovskites. I. geometrical considerations, Acta Crystallogr. B Struct. Sci. 53 (1) (1997) 32–43.
[47] P.M. Woodward, Octahedral tilting in perovskites. II. Structure stabilizing forces, Acta Crystallogr. B Struct. Sci. 53 (1) (1997) 44–66.